

Chapter 2

THE IMAGING FABRY-PÉROT SPECTROMETER (IFPS)

History of Fabry-Pérot spectrometer dates back to the late 19th century, when it was invented and used to calibrate the length of standard metre with the Cadmium line by Fabry and Pérot (1899). It was, however, Buisson and Fabry (1914) who first initiated the use of Fabry-Pérot spectrometers in astronomical studies, by making observations on the Orion Nebula.

With the technological developments in the following decades, capabilities of Fabry-Pérot spectrometer received a boost and it has found a wide-ranging applications in astronomy. It has become an important tool to extract kinematic information in extended astronomical sources like HII regions, Planetary nebulae and galaxies as well as comets and solar corona. The concentric

fringe system from a Fabry-Pérot étalon has a unique advantage for obtaining spectroscopic images as each point on any circular fringe corresponds to a spatial position on the sky. This advantage combined with the facility of wavelength scanning of the étalon is quite useful in the spectroscopy of extended sources. One can also use the étalon for obtaining emission line profiles over a limited spatial region (especially for point sources or in cases when a two-dimensional detector is unavailable) by selecting only the central fringe and scanning in wavelength.

Studies were carried out both in central fringe scanning mode using photoelectric techniques (e.g. Foukal, 1969) as well as in the two-dimensional interferometric mode for spatial information using essentially unaided or aided (with image intensifier tubes) photographic techniques (Courtés, 1960; Monnet, 1971; Tully, 1974; de Vaucouleurs and Pence, 1980). Recent developments in the two-dimensional digital panoramic detectors such as Charge-Coupled Devices (CCD), Imaging Photon Counting Systems (IPCS), Imaging Photon Detector (IPD) have brought a resurgence in the field of astronomy. These imaging detectors combined with the servo-controlled piezo-étalons (in which the étalon gap is created by spacers made of piezoelectric materials) have led to the development of Imaging Fabry-Pérot spectrometer systems - TAURUS (Atherton et al, 1982), CIGALE (Boulesteix et al, 1983), HIFI (Bland and Tully, 1989). We have designed and constructed one such Imaging Fabry-Pérot Spectrometer (IFPS) using Imaging Photon Detector (IPD). The following sections will give the details about the Fabry-Pérot Spectrom-

eter (FPS) and the fabrication, performance and important characteristics of the IFPS.

2.1 Theory and Definition of FPS

Detailed theory and practice of the Fabry-Pérot spectrometer is discussed in the excellent books by Born and Wolf (1970), Meaburn (1976), Hernandez (1986) and Vaughan (1989). Some of the important and relevant features for its selection for the present studies will be discussed in this section.

A Fabry-Pérot étalon essentially consists of a set of nearly perfectly flat ($\lambda/100$) parallel plates with their internal surfaces coated for high reflectivity ($\geq 90\%$) in a given range of wavelengths. An incident monochromatic beam of light of wavelength λ from an extended source when passed through the étalon would undergo multiple internal reflections. The emerging beams in transmission would then give rise to a set of concentric circular fringes of maxima when there occurs constructive interference with the following condition:

$$2\mu t \cos\theta = n\lambda \quad (2.1)$$

where μ is the refractive index of the medium between the plates of the étalon, t the gap between them, θ the angle of incidence, and n the order of interference. Each point on the fringe corresponds to a specific region in the extended object on the sky. The resulting transmission pattern is a train of periodic pulses each of which can be given by what is known as the Airy

function

$$A(\lambda) = \left\{ 1 + \left[\frac{4R}{(1-R)^2} \sin^2 \left(\frac{2\pi\mu t \cos\theta}{\lambda} \right) \right] \right\}^{-1} \quad (2.2)$$

where R is the reflectivity of the coatings. The following are some of the most important parameters that characterize the FPS.

1. Free Spectral Range: The period of the Airy function is known as the free spectral range (FSR) of the FP which gives the range in wavelength between two successive maxima and can be defined from eqn. 2.1 as

$$\Delta\lambda = \frac{\lambda^2}{2\mu t} \quad (2.3)$$

2. The full-width at half maximum: The full-width at half maximum (FWHM) of the peak defines the resolving power of the instrument and for high reflectivity it is given as (eqn. 2.2),

$$\delta\lambda = \Delta\lambda \frac{(1-R)}{\pi\sqrt{R}} \quad (2.4)$$

As is clear, a large value of the reflectivity R assures a small $\delta\lambda$ and hence a high resolution.

3. Finesse: The ratio of FSR to FWHM defines the finesse of the Fabry-Pérot spectrometer. The coefficient of reflective finesse is given as

$$N_R = \frac{\Delta\lambda}{\delta\lambda} = \frac{\pi\sqrt{R}}{1-R} \quad (2.5)$$

Finesse, in general, represents the number of interfering beams or the number of resolvable spectral elements in one FSR. A large finesse is assured if the reflectivity is greater than 90%.

4. Contrast: The contrast C is defined as the ratio of the transmission at the maximum of a passband to the transmission at the minimum between passbands

$$C = \left[\frac{1 + R}{1 - R} \right]^2 \quad (2.6)$$

This is a crucial parameter especially when continuum from the source becomes significant. Here too, a large R generates a large C .

5. Resolving Power: Two profiles of equally intense lines separated by $\delta\lambda$ are said to be resolved if the intensity in the dip of the resultant profile is 83% of the peak intensity (which is in close agreement with the Rayleigh criterion for resolving two closeby spectral lines).

The resolving power of FP étalon is given as:

$$R_p = \frac{\lambda}{\delta\lambda} = nN_R \quad (2.7)$$

In practice, there are deviations from perfect parallelism and flatness of plates of Fabry-Pérot combining with the fact that we use a finite aperture size resulting in the broadening of the instrument function and hence deteriorating the resolving power. Therefore, the instrument function is a convolution of Airy function $A(\lambda)$, aperture function $F(\lambda)$ and defect function $D(\lambda)$

$$I(\lambda) = A(\lambda) * F(\lambda) * D(\lambda) \quad (2.8)$$

Let us now examine briefly various defects contributing to the deterioration of the parallelism.

1. Plate defects: The plate defects are generally caused due to three factors (Atherton et al, 1982) as described in the following:

(i) Curvature effect: The plates in general, could have a curvature and hence be bow shaped in parts with a maximum excursion from the plane surface of δt , then the finesse due to this effect is

$$N_{DC} = \frac{\lambda}{2\delta t} \quad (2.9)$$

(ii) Broadening due to surface irregularities or microtopographic polishing errors is assumed to follow a Gaussian distribution and the corresponding finesse is,

$$N_{DG} = \frac{\lambda}{\delta t_G \times 4.7} \quad (2.10)$$

(ii) The finesse corresponding to broadening due to departure from parallelism (for a wedge shaped gap) is given by:

$$N_{DP} = \frac{\lambda}{\delta t_p \times \sqrt{3}} \quad (2.11)$$

Combining the above three, the effective defect finesse N_D is given by:

$$\frac{1}{N_D^2} = \frac{1}{N_{DC}^2} + \frac{1}{N_{DG}^2} + \frac{1}{N_{DP}^2} \quad (2.12)$$

2. Effect of finite aperture: The use of finite aperture results in the broadening of the instrument function which is defined as a rectangular function given as :

$$N_A = \frac{2\pi}{n\Omega} \quad (2.13)$$

where Ω is the solid angle subtended at the FPS.

Therefore the total effective finesse is given as follows:

$$\frac{1}{N_E} = \left[\frac{1}{N_D^2} + \frac{1}{N_R^2} + \frac{1}{N_A^2} \right]^{1/2} \quad (2.14)$$

If N_R is greater than N_D , the result is that of a series of FPS's arranged parallelly transmitting at slightly different wavelengths which results in a considerable reduction in the transmission at a particular wavelength though the bandwidth is narrower. Similarly, if N_D is increased, thereby increasing the amount of incident flux, there will be a decrease in N_A and the width of the transmission profile is broadened. The optimum product (bandwidth \times flux) will be obtained when

$$N_R \sim N_A \sim N_D \quad (2.15)$$

2.1.1 Merits

1. Firstly, the Fabry-Pérot spectrometer has large light gathering power. It was shown by Jacquinot (1954) that the flux F transmitted by any optical system is the product of the luminance L at the entrance aperture and the throughput α of the system. The luminance is defined as the intensity per unit area at the entrance slit and the throughput is the product of the solid angle Ω of the entrance slit subtended at the collimator, the collimator area S , and the spectrometer transmittance τ .

Jacquinot, by comparing luminosity-resolution product of different dispersive elements, found that for a specified resolution, the solid-angle

subtended at the FPS is much larger (as also for Michelson interferometer) than that in other dispersive elements such as grating and prism. Therefore, the quantity $L \times R_p$, which is a figure of merit (for any dispersive element), is found to be

$$L \times R_p = 2\pi S\tau R_p \quad (2.16)$$

and it was found that

$$(L \times R_p)_{FP} \approx 35(L \times R_p)_{Echelle} \quad (2.17)$$

$$\approx 30 \text{ to } 100(L \times R_p)_{Grating} \quad (2.18)$$

$$\approx 300 \text{ to } 1500(L \times R_p)_{Prism} \quad (2.19)$$

2. Secondly, observations with Imaging Fabry-Pérot spectrometer (IFPS) allow two-dimensional mapping of the velocity fields in astronomical objects, an advantage over slit spectroscopy which limits observations only along the length of the slit. Therefore imaging of the source in a single narrow spectral element can be obtained.
3. Thirdly, scanning of the Fabry-Pérot in wavelength results in the expansion/contraction of the fringes thereby covering the entire field of view of the object and providing accurate line profiles almost at each spatial element.

2.1.2 De-merits

1. The main constraint with Fabry-Pérot spectrometer is its limited free

spectral range which is to be selected depending on the width of the line of interest in the astronomical objects.

2. The Fabry-Pérot spectrometer has one more disadvantage of its ill-defined instrumental profile, particularly in the wings, caused due to the continuum leakage.

2.2 Design and Fabrication of IFPS

The following section describes the optical lay-out of the IFPS, the detector used and the data acquisition system.

2.2.1 Choice of the étalon parameters

One of our main criteria in designing the IFPS has been to map reasonably large regions in extended sources. The details of the Fabry-Pérot étalons to be used are given in Table 2.1. The number of fringes that can be obtained for each étalon type as permitted by the optics chosen is listed in Table 2.2. The FSR of the étalon is selected to be large enough so as to cover the velocity structure of the envisaged source. In the case of HII regions, the Doppler velocities are at maximum ~ 100 km/s. Therefore the étalon is chosen with FSR of ~ 180 km/s (ET2) which is adequate for the present work. The effective finesse is ~ 30 , giving a resolving power of 5×10^4 at $\lambda = 5007 \text{ \AA}$ (Table 2.1).

Table 2.1: Parameters of Fabry-Pérot Étalons for use with the IFPS

Etalon	FSR ($\text{\AA}/\text{km s}^{-1}$)	Resolving ^a Power(R_p)	Wavelength Region(\AA)	Velocity Resolution ($\text{\AA}/\text{km s}^{-1}$)	Etalon type
ET1 PET 85	4.3/196.6	4.5×10^4	6000-7000	0.146/6.6	PZ ^b
ET2 PET 50	3.0/179.7	5.0×10^4	4500-5500	0.100/6.0	PZ
ET3 PET 28	22.2/1014.8	8.9×10^3	6000-7000	0.737/33.7	PZ
ET4 PET 28	10.2/466.2	1.9×10^4	6000-7000	0.345/15.8	PZ
ET5 OET 45	11.9/544.0	6.0×10^3	6000-7000	1.094/50.0	OC ^c
ET6 OET 20	21.5/982.8	9.0×10^3	4400-8400	0.171/32.8	OC

^aThe values given in the table are computed using $\lambda = 6563 \text{ \AA}$ except for ET2 for which $\lambda = 5007 \text{ \AA}$.

^bPiezo-electrically scanned.

^cOptically contacted.

Table 2.2: The number of fringes for each étalon type that can be imaged on IPD at a given scanning step

Etalon	Peak wavelength (\AA)	number of fringes
ET 50	5007	~ 5
ET 85	6563	~ 4
ET 28	6563	~ 2
ET 28	6563	~ 1

2.2.2 Optical system

A schematic lay-out of the instrument is shown in Fig 2.1. The Cassegrain beam from a telescope (1.21 or 2.3m, $f/13$; 35cm, $f/11$) first passes through a field aperture which isolates the desired region of the astronomical object under investigation. The field aperture consists of an iris diaphragm which can be set anywhere between 1.4 and 18 mm, whereby the field of view can be estimated from the plate factor values of $50''$, $13''$ and $6.8''/\text{mm}$, for the 35 cm, 1.21 and 2.34 m telescopes, respectively. Object acquisition, centring and focusing in the field aperture is facilitated by both a pre-aperture, large field-of-view eyepiece, and also a second post-aperture eyepiece (with a smaller field-of-view). A flip mirror allows the light from a spectral lamp to enter the instrument for taking frames for calibration and evaluation of instrument performance, as well as to view the object in the eyepiece. The beam is then collimated by an achromatic lens of focal length 120 mm and after pre-filtering by a suitable image-quality interference filter, centred on any chosen spectral line of emission, passes through the étalon. The camera lens of focal length 120 mm images the fringes onto the detector (IPD) kept at its focal plane with a beam of $f/6.7$. Another aperture near the detector acts as a baffle to avoid ghost images. Also a provision has been made to tilt the FP étalon in order to throw the ghost images out of the detector's area. The design and selection of the various optical elements have been made in such a way as to minimize the vignetting effects even for the largest aperture to be used, viz. 18 mm. In designing the IFPS, it is seen that the angular

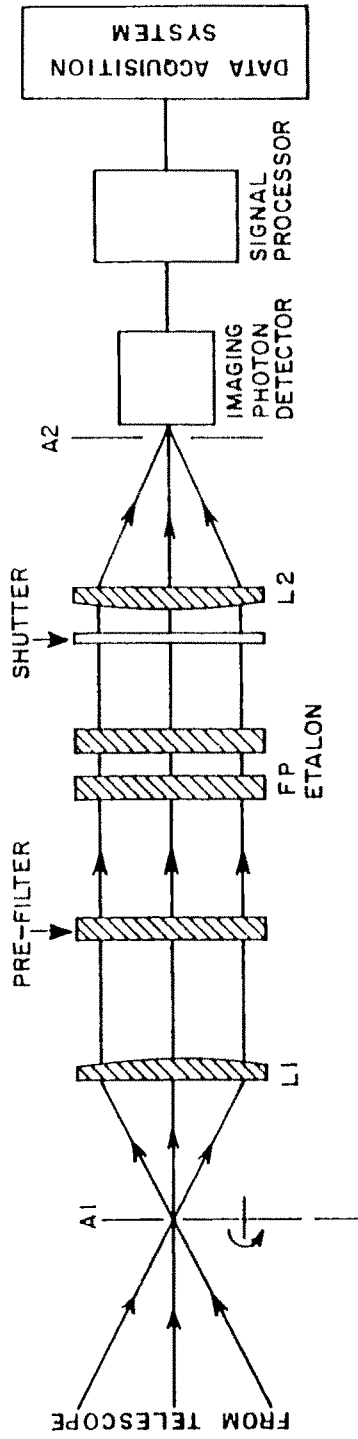


Figure 2.1: Schematic layout of Imaging Fabry-Pérot Spectrometer (IFPS).



Table 2.3: Width (FWHM) of interference fringes as imaged on the IPD covering at least one pixel (for ET2 PET 50).

Order	θ (degrees)	number of pixels
1661	1.63	2.2
1660	2.58	1.4
1659	3.26	1.2
1658	3.81	1.0

dispersion (variation of λ with θ) across an off-axis pixel (at the maximum angle from the normal) should not exceed $\delta\lambda$. This can be justified from Table 2.3 which shows that the fringe width $\delta\lambda$ of the interferogram covers at least one pixel, thus,

$$(\delta\lambda)_\theta = \frac{\lambda p}{f_{cam}} \tan \theta \leq \delta\lambda \quad (2.20)$$

where p is the size of the pixel and f_{cam} is the focal length of the camera imaging lens.

2.2.3 Scanning the IFPS

As mentioned earlier, the real advantage of the FPS comes about in terms of scanning the étalon so as to sample larger regions of the object which are not covered in a single interferogram and thus line profiles from each spatial point of the object can be obtained accurately. This becomes possible in the case of digital panoramic detectors because of their higher sensitivity and

ease in recording the data.

Before the development of piezo-étalons, scanning was done by changing the refractive index of the gas between the plates (pressure scanning). This method of scanning is rather cumbersome and has the limitations due to the dynamic range available in the gas pressure, restricting the scanning range to be less than 20 Å (Atherton et al, 1982). Also, there is a possibility of leakage of gas through the FP chamber at high pressure. With the development of piezo-electric étalons, scanning was made possible by changing the étalon spacing and maintaining the plate parallelism using servo-controlled capacitance micrometry (Jones and Richards, 1973). Earlier on, feedback systems utilized light beams for detecting the errors in the signals, which restricted the observations to only bright sources.

The étalon is piezo-electrically scanned and servo-controlled using the CS-100 servo control unit supplied by the Queensgate Instrument, U.K. The CS-100 system utilizes the principle of capacitance micrometry developed by Jones and Richards (1973) which allows pico-metre displacements to be detected. The interferometer plates are held apart by three piezo-electric transducers. The étalons are connected with five capacitors formed by evaporating gold pads onto one of the interferometer plates and fused silica pillars optically contacted to the étalon base plate. These five capacitors are mounted on one of the étalon plates in such a way that two pairs form two mutually perpendicular axes and the fifth one serves as reference. The capacitance micrometers sense variations in parallelism and departures from required

spacing. The CS-100 system receives the error signal from the capacitance micrometers and sends back appropriate voltage to the piezo-transducers for maintaining the parallelism. Thus, CS-100 system utilizes a closed-loop feedback system and maintains parallelism to better than $\lambda/2000$; correcting errors in typically less than 0.3 ms (Atherton et al, 1982). Piezo-electric transducer sensitivity is 2.4 nm/V.

The scanning steps, step-sizes and integration times are controlled by a personal computer interfaced (RS 232) with the CS-100 by using a software developed by us. The step number is a function of plate spacing and can be varied in the order of 1, 2, 3 ... depending on the requirement of the observations. To scan one order in wavelength, the plate gap is required to be changed by $\lambda/2$ i.e., the gap should be changed by 2500 Å at the wavelength of 5000 Å or by 512 steps of step size 1. The smallest increment of plate separation adjustments is 0.5 nm or 1/500 of a Fabry-Pérot order at a wavelength of 5000 Å (CS-100 manual). The full drive available for the piezo-electric transducers is $\pm 750V$ (1800nm).

2.2.4 Interference filters

Image quality interference filters were used for the present observations. They are different from the ordinary filters in the sense that they are a single component system in which coatings are deposited on a single surface to eliminate any ghost or multiple imaging. Both exterior surfaces are anti-

Table 2.4: Characteristics of the interference filter used

Type	Image quality Interference filter (Spectro Film Inc.)
Size	Circular (dia = 2 inch)
Peak transmission wavelength	5010 Å
FWHM	20 Å at 20°C for [OIII] 5007 Å
Temperature Coefficient	0.15 Å red shift/°C
Peak transmission	40-50%

reflection coated. The filter bandwidths are chosen to be greater than the FSR of the FPS. Details of the interference filters used are given in Table 2.4.

2.3 Detectors

The efficiency or capability of any detector is governed by its characteristic properties, viz. the quantum efficiency, the dynamic range and the spectral response (Kitchin, 1991).

Until the 17th century the unaided human eye served the purpose of a detector. It is capable of covering the optical range from 4000 Å to 7000 Å. The eye is supposed to be able to resolve angles of one minute of arc but is incapable of storing or making a permanent record of the image. There were instances, thus, of astronomers recording sketches of the eye-witnessed pictures of celestial objects that are bright and large in angular size. In the late

19th century, the art of photography was developed and became the chief detection as well as data acquisition system in astronomy. A photographic film consists of an emulsion of silver halide (mainly bromide) crystals in gelatin, deposited on a plane glass plate or a celluloid sheet in a thin uniform layer. The interaction of the infalling light photons and the emulsion results in the production and accumulation of silver ions where ever the light was incident on the emulsion. Photographic plates are found to be sensitive in the whole of the optical spectrum except in the infrared region beyond 12000 \AA . Because of its capability of integrating over a long time, it had proved to be a useful tool for the studies of weak astronomical sources. But a major limitation of photographic plates is its low sensitivity and the complex method involved while analyzing the signal, since the data is not accessible immediately for analysis. The photographic plate is to be processed first and the density is recorded by using a microdensitometer which is then related to the transmittance according to the relation $D = -\log T$, where D , is the density of silver ions formed on irradiation by photons, and T is the transmission of the film. Each plate requires a characteristic curve of density verses $\log E$ (transmittance \times exposure time) which gives the required conversion factor from density to intensity. Therefore the analysis procedure becomes quite complex.

With the development of technology, photoelectric detectors called photomultiplier tubes (PMTs) were manufactured. The photomultiplier tube exploits the principle of photoelectric effect. When the electromagnetic ra-

diation is incident on a negatively charged electrode (the cathode), photoelectrons are liberated which are then accelerated to a positively charged electrode (the anode). The amplification of the signal in the PMT is achieved by means of electron multipliers called dynodes. Dynodes are given progressively higher positive potentials and are arranged in such a fashion that the electrons leaving one dynode are directed towards the next. Successive multiplications will therefore result in an exponential growth in the signal. The gain in the signal is in the range of 10^6 to 10^8 .

The quantum efficiency of the PMTs varies from ultraviolet to far-red and at best it is 20% at 5000 Å. But, the shortcoming of a PMT is that it can sample only an integrated small portion of the sky at a time. Therefore, extended objects such as Planetary nebulae, HII regions and galaxies must be sampled part by part, requiring large amounts of telescope times.

With the aim to combine the spatial recording ability of the photographic plate and the reasonably good quantum efficiency of PMT's, Image Intensifiers were developed. An Image Intensifier is a vacuum tube with two electrodes, a negatively charged electrode, the cathode and a positively charged electrode, the anode. The cathode and anode are kept close together to preserve the spatial resolution. The photoelectrons liberated by the photocathode are accelerated to the anode following paths that are approximately straight lines. The anode is made of a fluorescent material in order to produce visible output. In order to increase the electron gain, Microchannel Plates (MCPs) are incorporated in the Image Intensifiers. MCPs comprise

Table 2.5: Comparison of the characteristic properties of different detectors

Characteristic property	Photographic plate	PMT	CCD	IPD
Quantum efficiency (visible range)	1%	10-20%	20-70%	10-20%
Dynamic range	~ 100	$\sim 10^6$	$\sim 10^4$	$\sim 10^{5^a}$
Spectral response(μm)	0.3-0.7	0.2-1.0	0.4-1.1	0.2-1.0

^aThis is true provided number of counts in each pixel do not exceed 100/s.

of millions of miniature PMTs arranged in two-dimensional array.

Recent developments in the microelectronic technology has led to the advent of digital panoramic two dimensional detectors like charge coupled devices (CCDs) and imaging photon counting detectors (IPCS & IPDs). The spectral response, quantum efficiency and sensitivity of different light detectors are compared in the Table 2.5. In what follows, we give details of an imaging photon-counting detector that is used in our IFPS.

2.3.1 Introduction to Imaging Photon Detector (IPD)

The imaging photon detector (IPD) is a two dimensional sensor capable of detecting a single photoelectron. It consists of a S-20 photocathode, a stack of three microchannel plates and a position sensitive resistive anode. A schematic layout of IPD is shown in Fig. 2.2.

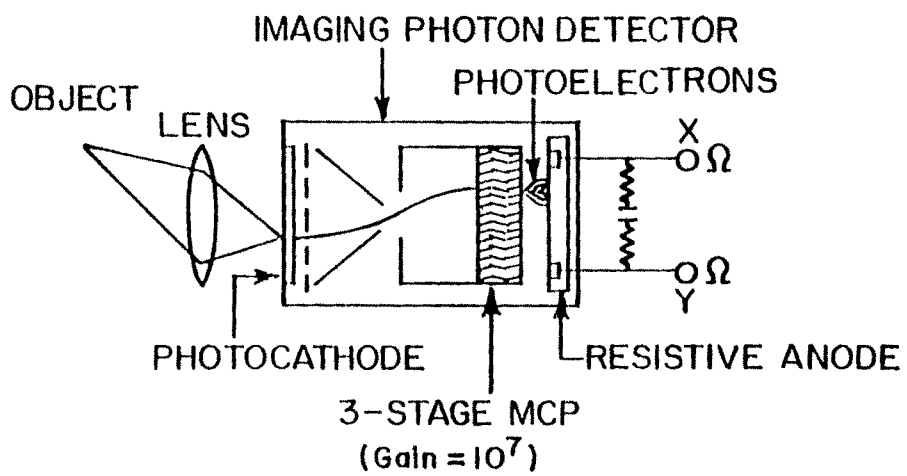


Figure 2.2: A schematic layout of Imaging Photon Detector (from Tsuchiya et al, 1985).

The IPD system comprises of (i) Detector unit and (ii) Processing electronics.

Principle of operation

Photoelectrons released from the photocathode are drawn to the microchannel plates (MCP) by means of the electric field applied across the gap. The cathode is proximity focussed to the MCP. On entering one of the microchannels, a primary photoelectron strikes the channel wall, liberating a shower of secondary electrons which are all accelerated down the channel, hitting the wall and producing further secondary electrons in the process.

The electron gain achieved is up to 10^7 electrons per event. The electrons are drawn by a weak electric field to the resistive anode. The resistive anode has four arc-terminating resistors at the four corners which create the effect of an infinite sheet (for details, Lampton et al, 1979) as shown in Fig. 2.3. When a charge cloud strikes the anode, a fraction of the charge leaves from each of the four corners connected to the virtual earth. The pulses are amplified by fast preamplifiers, shaped and buffered and fed to the processing unit. The electronic processor unit analyzes the signals from the resistive anode and gives the X,Y information along with a strobe pulse to an image acquisition and processing system which can be set to an integration time of our choice. The position of photon event is determined as a function of the amount of

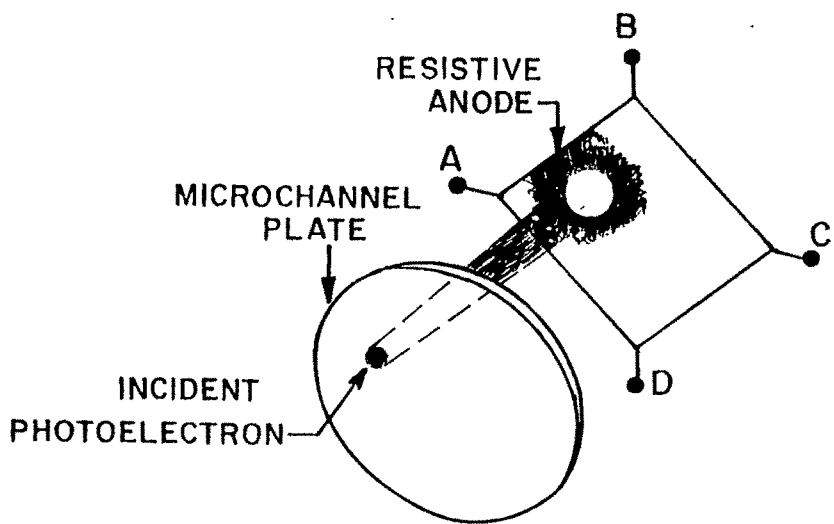


Figure 2.3: A resistive anode (from Lampton, 1981).

current measured at the four corners of the electrodes (I_1 through I_4):

$$X = \frac{I_1 + I_3}{I_1 + I_2 + I_3 + I_4}$$

$$Y = \frac{I_2 + I_4}{I_1 + I_2 + I_3 + I_4}$$

Characteristic features

The limitations on the detector are that there is a dead time of about $7 \mu\text{s}$ during which the electronic unit analyses the signals and hence no second signal would be allowed. This restricts the count rate to about 1.4×10^5 counts/s on the entire detector. Also, the conductivity of the microchannels limits the maximum counts in a given area of around $60 \mu\text{m}$ to about 100 counts/s. Since IPD, in our case, is used only after a filter and FP in the optical system, this limitation (of maximum count rate) does not affect the observations. There is an uncertainty in the centroiding of an event at the resistive anode which gives rise to the concept of a circle of least confusion and thereby also defines a pixel size for the IPD. Using a chromium positive test target (ruled with different sets of line pairs per mm), we have estimated the pixel size to be about $60 \mu\text{m}$. For this pixel size, there would be 9×10^4 pixels (300×300 in circular array) associated with the IPD. These characteristic features are summarised in the Table 2.6. The spectral response curve of IPD is shown in Fig. 2.4. Fig. 2.5 shows the resolution versus illuminance for IPD in comparison with a CCD.

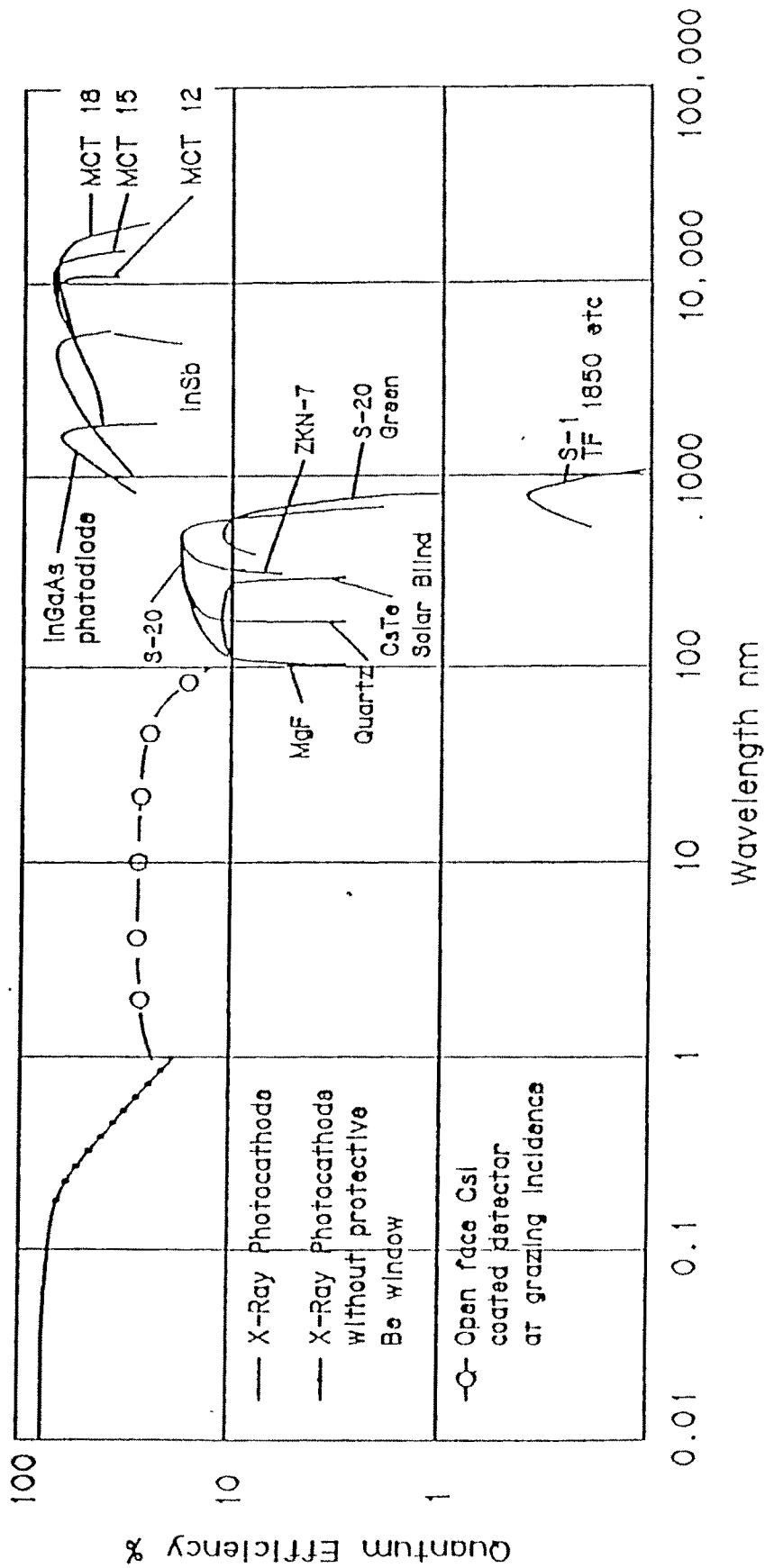


Figure 2.4: Spectral response curve of IPD (marked S-20).

LIGHT LEVEL ON THE FACEPLATES

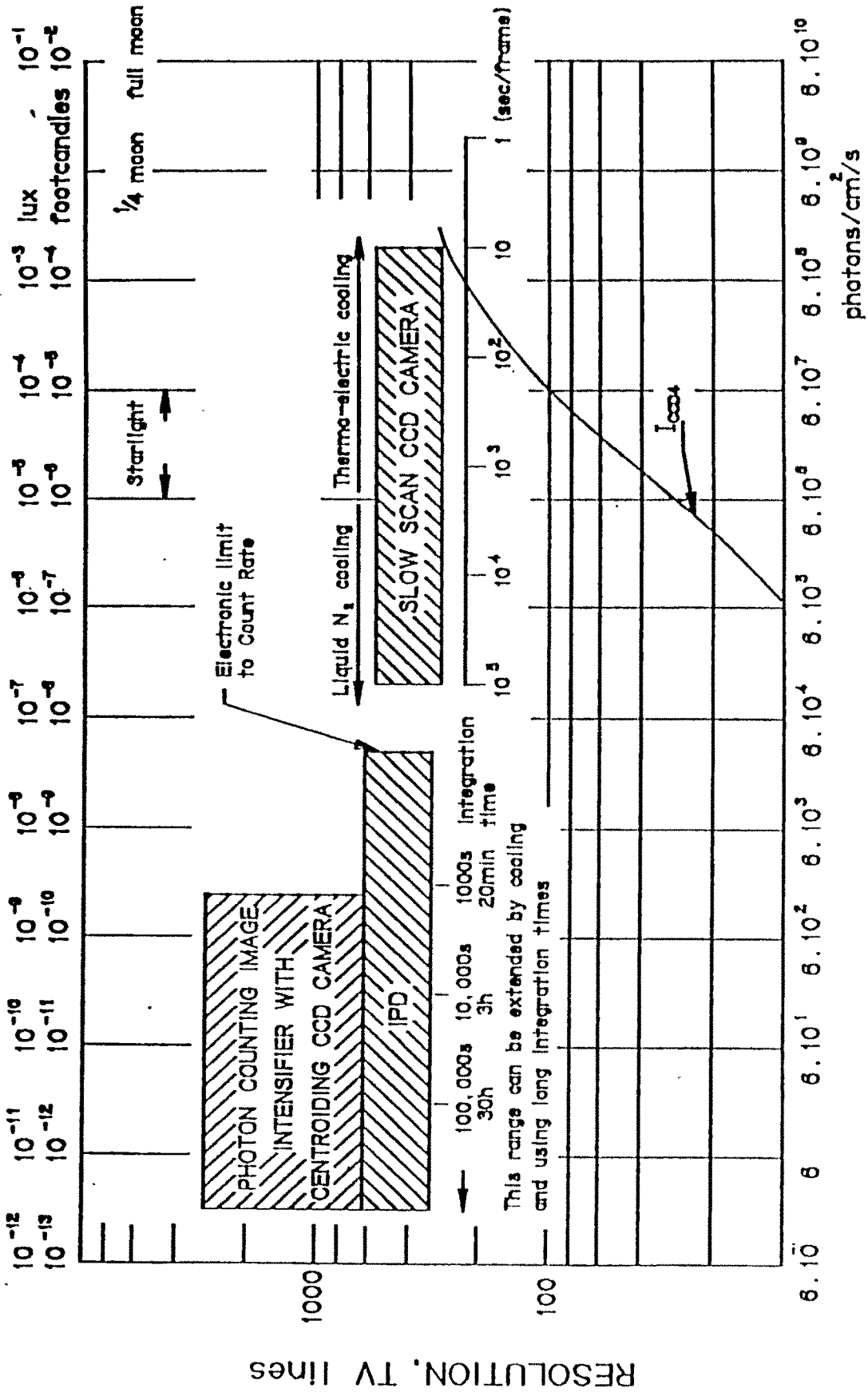


Figure 2.5: Resolution versus illuminance for IPD & CCD

Table 2.6: Characteristics of the IPD

Photocathode	S-20
Active Diameter	18 mm
Quantum efficiency at 5000 Å	18%
Resolution	60 μ m
Microchannel plate gain	10 ⁷
Maximum Count rate	10 ⁵ events/s
Dark noise at 20°C	4 × 10 ⁻³ counts/s/pixel
Total number of pixels	300 × 300(9 × 10 ⁴)
Dead time	7 × 10 ⁻⁶ s

The optical design chosen by us permits the following spatial resolution for different telescopes: for an image at the f/13 Cassegrain focus of the 2.34m and 1.2m telescope, we obtain 0.41 arcsec and 0.78 arc sec per pixel respectively, whereas for f/11 Cassegrain focus of the 35cm telescope, each pixel corresponds to about 2.0 arcsec.

Sources of noise and pulse height distribution

The pulse height is actually controlled by the MCP voltage and is set by the upper and lower thresholds. The small noise pulses generated by Johnson noise (within the position sensitive anode itself) and electronic noise (generated in the charge sensitive preamplifiers) are rejected by the lower threshold and large pulses such as those generated by coincident events, ions, cosmic rays etc are cut off by the upper threshold. Fig 2.6 shows a typical pulse

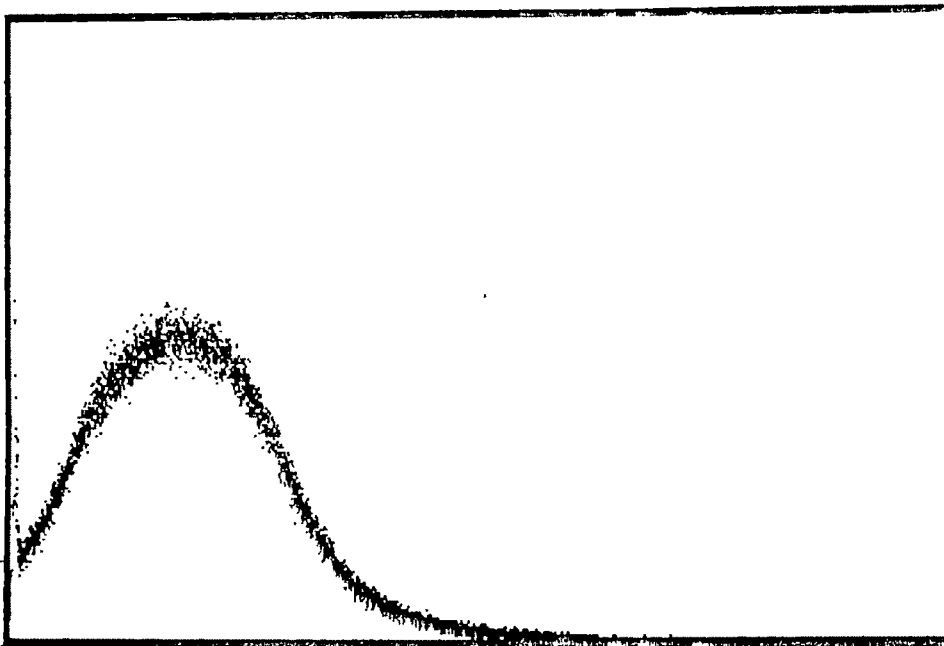


Figure 2.6: Pulse height distribution as obtained for the 18mm IPD in the illuminated condition. The x-axis runs from 0 to 8 V and y-axis shows the number of counts (arbitrary units).

height distribution we have obtained for the 18mm diameter IPD in the detector illuminated condition.

Estimation of Integration times

Theoretical estimates of the integration times required for obtaining reasonably good S/N ratios ($S/N = s \times [t/(s + d)]^{1/2}$, where s and d are source and dark counts per second and t is the time of integration in seconds) for objects of different fluxes in H_α are given in Table 2.7. The transmittivity of the entire instrument is taken to be $\sim 20\%$ and the quantum efficiency of the detector $\sim 7\%$ at $\lambda = 6563 \text{ \AA}$. The fluxes are taken from Kennicutt and Kent (1983) to evaluate the integration time.

A comparison with other types of Imaging detectors

The imaging Fabry-Perot spectrometer 'TAURUS' developed by Atherton et al (1982) utilises an Imaging Photon-Counting System (IPCS, Boksenberg, 1972) while the recent system developed by Bland and Tully (1989) uses a CCD. IPCS works on a similar principle as IPD except that a videcon tube replaces the resistive anode for position detection (Boksenberg, 1972). IPD is far smaller and lighter compared to IPCS and does not require expensive and clumsy water cooling and focussing solenoid power supplies.

The comparison of IPD with CCD requires comparison of the readout

Table 2.7: Theoretical estimates of integration times for different sources
S/N=10 with a 2.3 m telescope using the IFPS

Object NGC	Type	Apparent magnitude	H α flux (erg cm $^{-2}$ s $^{-1}$ arcsec $^{-2}$)	Integration time (min)
628	Galaxy SA(s)	9.6	9.3×10^{-17}	40
3310	Galaxy SAB(r)	11.2	4.8×10^{-16}	2
3504	Galaxy SAB(s)	10.7	1.4×10^{-16}	25
4736	Galaxy SA(r)	8.1	10.2×10^{-17}	40
4790	Galaxy SB(rs)	12.5	9.5×10^{-17}	40
5055	Galaxy SA(rs)	8.9	10.7×10^{-17}	40
5194	Galaxy SA(s)	8.4	2.2×10^{-16}	8
6853	Planetary Nebula	8.1	$1.4 \times 10^{-14}^a$	2

^aFlux is for the [OIII] 5007 Å line (Barker, 1984) and the integration time is for the brightest portion of a beam $\sim 1'$ only.

noise and the readout time of CCDs with the dark noise and the dead time of the electronics in IPDs respectively. A detailed discussion with respect to this can be found in the literature (Mackay 1986; Jenkins 1987; Bland and Tully 1989). Currently available high resolution CCDs have readout noise of a few electrons per pixel but a readout time of a few tens of seconds (typically 60s). The dark noise in the IPD is typically 4×10^{-3} counts/s/pixel at 20° C, while the dead time is $\sim 7\mu\text{s}$. Whereas IPD has limitations on the maximum count rate (due to the dead time) of a few times $\times 10^5$ counts/s and a pixel count rate of a maximum of ~ 100 counts/s (due to the conductivity of microchannels), the CCD is free from such restrictions. Bland and Tully (1989) showed that in order to obtain a $(S/N)_c$ for CCD greater than $(S/N)_p$ for the IPD with the assumptions: (i) all the signal resides in the emission line; (ii) background sky noise is low and (iii) Signal/Noise > 3 , the following inequality should be justified,

$$(S/N)_p \leq 2.3\sqrt{1 + (\tau_R/\tau_o)} \quad (2.21)$$

where τ_R is the read out time and τ_o is the exposure time.

From eqn. 2.21, it is clear that for a short readout time CCD seems to be a better choice whereas for a short exposure time photon-counting detectors are more suitable. It therefore appears that the CCD basically scores over the IPD for long exposure times and hence for faint sources in the case of a single interferogram. Also, it is possible to have rapid scanning

in wavelength with photon counting device which will result in averaging the fluctuations in atmospheric transparency. But, for a CCD it is required to integrate for a longer time at each gap spacing till the photon statistics exceed readout noise. Therefore slow scanning only is possible in CCD's allowing observations covering only a few steps (Bland & Tully, 1989). Therefore, for scanning FPS, IPD is still preferred to the CCD.

2.4 Image data Acquisition System

The block diagram of the Image data acquisition system is shown in Fig. 2.7. The IPD sensor outputs A, B, C, D, are connected to the electronics processing unit (supplied by ITL, England). The electronics processing unit generates the X-Y coordinates information, for each photoelectron event detected in digital form, ten bits each of X and Y, together with a strobe pulse. The analog X-Y outputs from the electronics unit are fed to a storage oscilloscope to see the individual events in real time as a check that the detector is operating correctly.

The digital image is acquired and stored by the frame store unit using the IFS216 software (supplied by ITL). The image is displayed on the high resolution VGA monitor. The software enables the setting up of the required integration times for each frame. A micro-processor based computer card is developed by us and fixed in the PC computer for the operation and control of the system as per the requirement of the observations. It has the following

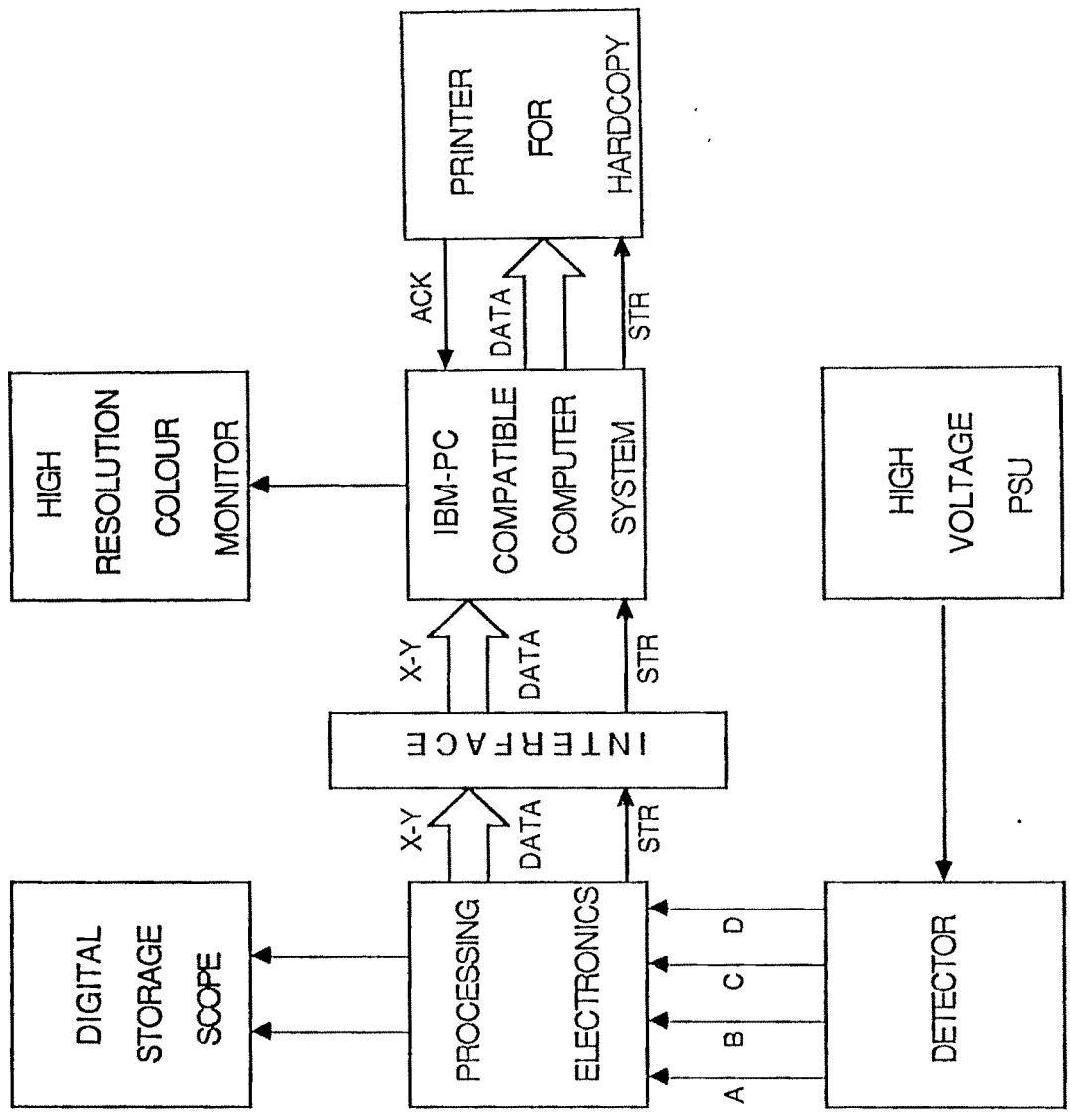


Figure 2.7: Block diagram of Image Data acquisition system

functions:

- Firstly, it inputs the wavelength of interest in order to choose the number of steps required for scanning through one FSR.
- The step size required for scanning of the étalon is given as an input parameter through the terminal.
- Next, it feeds the CS-100 unit with the required value of the step-size and waits for the acquisition of the image at each step.
- Immediately after the acquisition of the image is over, it sets the CS-100 to the next step and again an image is acquired and so on over one FSR.
- After completion of the scan for one FSR, the CS-100 unit is restored to its normal position.

2.5 Instrument Performance

A photograph of the completed IFPS set up in the laboratory with the CS-100 and detector (IPD) system is shown in Fig. 2.8. The performance of the instrument is tested by obtaining interferogram of standard laboratory source using the zinc spectral lamp, $\text{ZnI}4684.14 \text{ \AA}$ in green region and $\text{NeI}6598.9 \text{ \AA}$ in the red region. Fig. 2.9 shows interferogram in the zinc line. A radial scan taken from the centre of the interference fringes gave the instrument profile as shown in Fig. 2.10.



Figure 2.8: IFPS set-up in the laboratory.

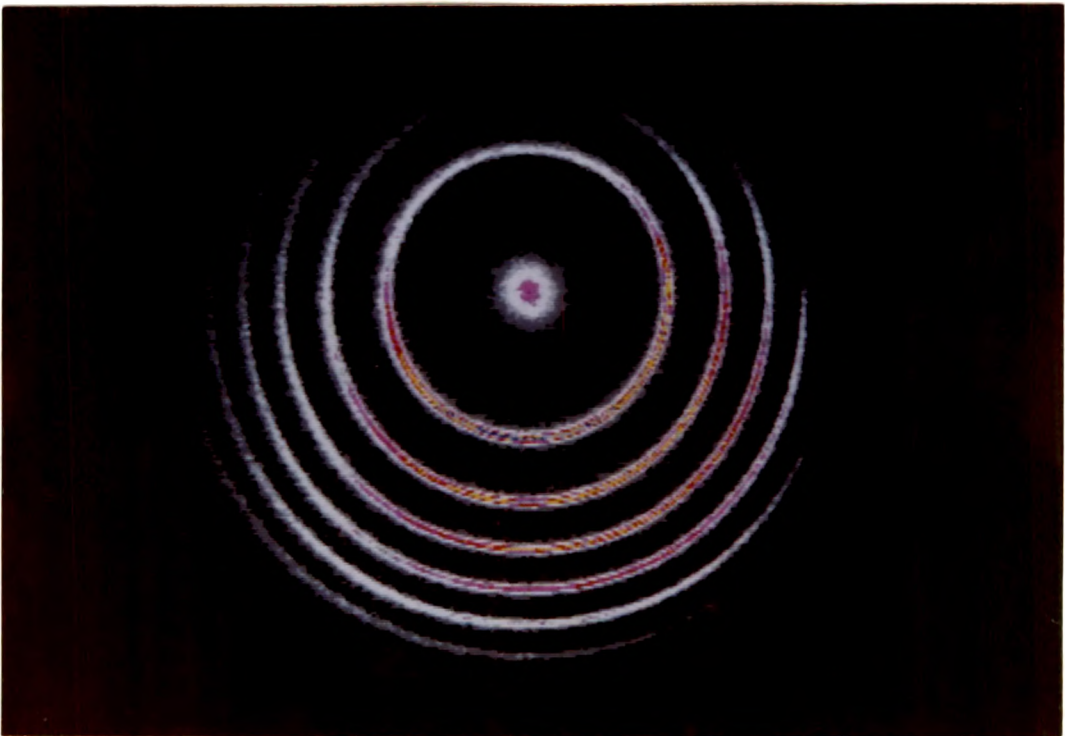


Figure 2.9: Interferogram obtained in Zn I line, $\lambda=4684.14 \text{ \AA}$, with integration of 1 minute.

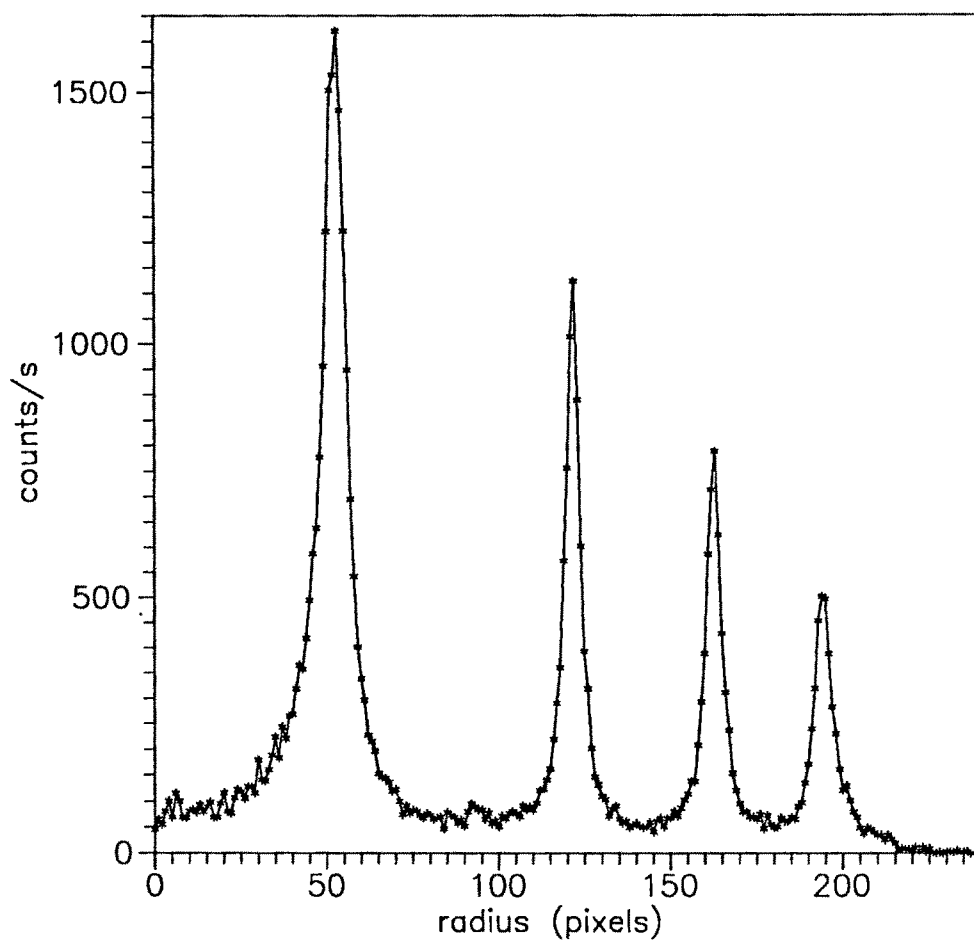


Figure 2.10: Radial scan from the centre of the interference fringes in Zn I line, $\lambda=4684.14 \text{ \AA}$

The reflective finesse for $\lambda = 5007 \text{ \AA}$, with reflectivity of 93% can be calculated from eqn. 2.5 to be 43.3. Considering the quoted plate flatness to be $\lambda/100$, N_{DC} is obtained as 50 from eqn. 2.9. Since the defect due to microtopographic polishing errors is not specified by the manufacturer, the defect finesse, N_{DG} is found to be 21 from eqn. 2.10, considering the error to be $\lambda/100$ and N_{DP} to be 150, plate parallelism being maintained at $\lambda/2000$ (eqn. 2.11).

Therefore, the overall defect finesse from eqn. 2.14 is found to be in the range $21 \leq N_D \leq 50$. The aperture finesse N_A is found to be 195 (eqn. 2.13) by taking solid-angle subtended by the aperture at a pixel to be $\sim 1.938 \times 10^{-5}$ steradians. The effective finesse from eqn. 2.14 is then found to be ~ 32 , which is in good agreement with the observed finesse ~ 30 found after deconvolving with the aperture function.

A profile is obtained at a single pixel using Ne I 6598.5 \AA line as shown in Fig. 2.11.

Observations made on certain HII regions (viz. Orion and Trifid) and Planetary nebulae (viz. Dumbbell) agree well with the theoretical estimates for the performance of the instrument shown in Table 2.7.

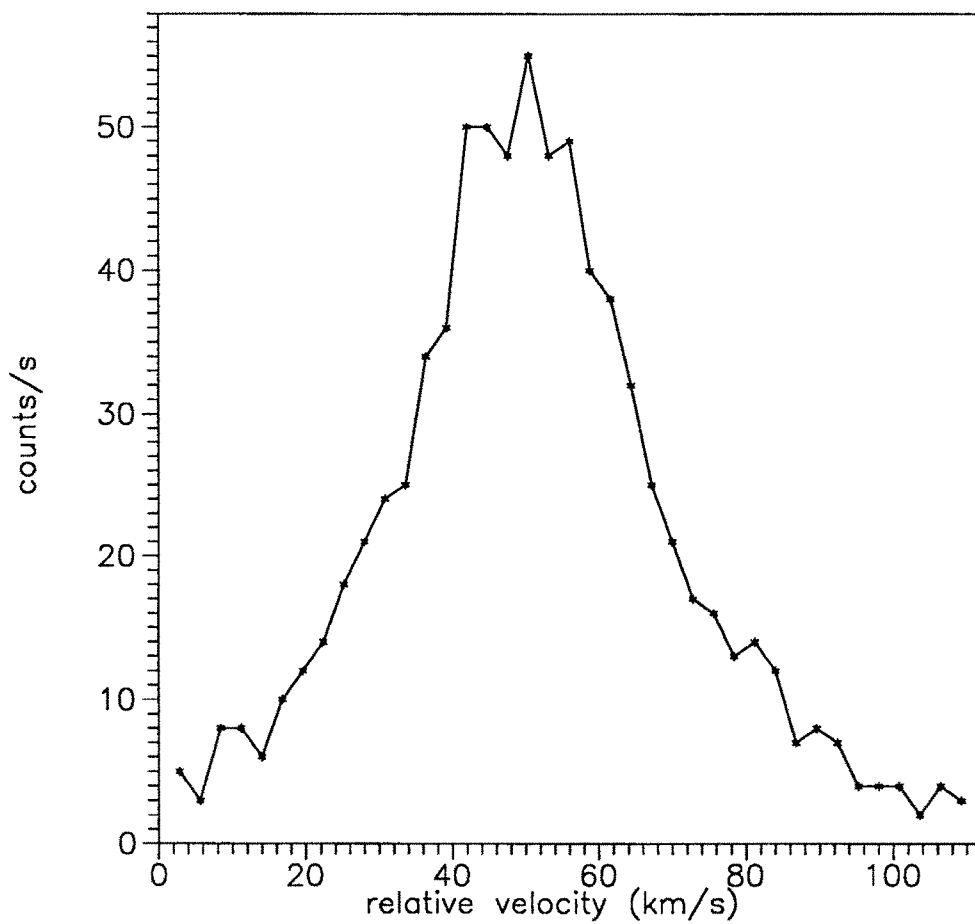


Figure 2.11: Line profile at a single pixel in neon line, $\lambda=6598.5 \text{ \AA}$.